MAGNETIC ADSORBENT BASED ON NANOCELLULOSE FOR OXYTETRACYCLINE REMOVAL: KINETICS, ISOTHERMS, AND THERMODYNAMICS

Đến tòa soạn: 22-05-2025

Pham Vu Nhat Uyen, Doan Van Dat, Nguyen Van Cuong*[*]

Faculty of Chemical Engineering, Industrial University of Ho Chi Minh City, Ho Chi Minh City, 700000, Vietnam

**E-mail: nvc@iuh.edu.vn*

TÓM TẮT

VẬT LIỆU HẤP PHỤ TỪ TÍNH TRÊN NỀN NANOCELLULOSE LOẠI BỎ OXYTETRACYCLINE: ĐỘNG HỌC, ĐẲNG NHIỆT VÀ NHIỆT ĐỘNG HỌC

Dư lượng Oxytetracycline (OTC) trong môi trường nước gây ảnh hưởng nghiêm trọng đến hệ sinh thái và sức khỏe cộng đồng. Nghiên cứu này giới thiệu vật liệu hấp phụ từ tính nền nanocellulose (Fe_3O_4@CNCs) được tổng hợp bằng phương pháp đồng kết tủa, sử dụng cellulose vi tinh thể (CNCs) chiết xuất từ rau nhút (Neptunia oleracea). Vật liệu được đặc trưng bằng SEM, EDS, FTIR, XRD, BET và VSM. Khả năng hấp phụ OTC được khảo sát trong các điều kiện pH, liều lượng, nồng độ, nhiệt độ và thời gian tiếp xúc khác nhau. Ở điều kiện pH 6 và 30 °C, hiệu suất loại bỏ đạt 89,08% với dung lượng hấp phụ 22,83 mg/g. Dữ liệu động học tuân theo mô hình bậc hai giả (R^2 = 0,9994), cho thấy cơ chế hấp phụ hóa học. Cả hai mô hình Langmuir và Freundlich đều phù hợp (q_{max} = 50,76 mg/g; R^2 > 0,98), phản ánh hấp phụ đa lớp trên bề mặt không đồng nhất. Các thông số nhiệt động học (ΔH = –24.03 kJ/mol; ΔG từ –7.98 đến –6.40 kJ/mol; ΔS = –52.96 J/mol·K) chỉ ra quá trình là tự phát, tỏa nhiệt và chủ yếu do tương tác vật lý. Vật liệu vẫn duy trì hiệu suất loại bỏ trên 70% sau ba chu kỳ tái sử dụng. Fe_3O_4@CNCs cho thấy tiềm năng cao trong xử lý nước ô nhiễm chứa kháng sinh.

Từ khóa: *Oxytetracycline, từ tính, nanocellulose, hấp phụ, xử lý nước*

1. INTRODUCTION

The excessive and often uncontrolled application of antibiotics in both clinical and agricultural contexts has led to the continuous discharge of pharmaceutical residues into natural water bodies [1-4]. Among these, oxytetracycline (OTC) is one of the most frequently detected antibiotics in wastewater, rivers, and lakes due to its extensive use and poor degradability [5, 6]. OTC is not only toxic to aquatic organisms but also poses a risk of promoting antimicrobial resistance, which has been classified as a critical global health threat by the World Health Organization [7, 8]. Therefore, the removal of OTC from aqueous environments is an urgent and important challenge in the field of environmental engineering [9, 10].

Traditional wastewater treatment systems, including biological and chemical processes, often failed to effectively remove OTC due to its stable molecular structure and strong affinity for organic matter [9, 11]. As a result, adsorption emerged as a promising method for antibiotic removal, owing to its simplicity, efficiency, low cost, and adaptability [12, 13]. However, the success of adsorption depended heavily on the design of high-performance adsorbent materials with sufficient surface area, functional group availability, and reusability [14-16].

Cellulose nanocrystals (CNCs), derived from renewable biomass, possessed numerous hydroxyl groups, high crystallinity, and large surface area, making them attractive candidates for use as green adsorbents [17]. Nevertheless, their direct application in water treatment remained limited by their lack of selectivity, aggregation tendencies, and difficulty in post-treatment separation. To address these limitations, the integration of magnetic nanoparticles, such as Fe_3O_4, into CNCs proved effective in improving both adsorption efficiency and recyclability [18-20]. The magnetic functionality enabled rapid separation from solution under an external magnetic field, while Fe_3O_4 nanoparticles introduced additional active sites and potential for specific interactions with target pollutants [21].

In this study, a Fe_3O_4-decorated CNCs composite (Fe_3O_4@CNCs) was synthesized via a facile co-precipitation method using CNCs extracted from the aerenchyma tissue of *Neptunia oleracea* (commonly known as water mimosa), a sustainable aquatic plant. The synthesized composite was thoroughly characterized using SEM, EDS, FTIR, XRD, BET, and VSM techniques to confirm its structure, morphology, surface area, and magnetic behavior [18, 20]. The adsorption performance of Fe_3O_4@CNCs toward OTC was evaluated under different operational conditions, including pH, adsorbent dosage, initial concentration, temperature, and contact time [22].

Furthermore, adsorption kinetics, isotherms, and thermodynamic analyses were carried out to elucidate the adsorption mechanism. The reusability and structural stability of the composite were also assessed through repeated adsorption–desorption cycles. The findings of this work aimed to provide a cost-effective, magnetically retrievable, and environmentally sustainable solution for the removal of antibiotic pollutants from water [23-26].

2. EXPERIMENT

All reagents used in this study were of analytical grade and used without further purification. Iron(II) sulfate heptahydrate ($FeSO_4 \cdot 7H_2O$, ≥ 99%) and iron(III) chloride hexahydrate ($FeCl_3 \cdot 6H_2O$, ≥ 97%) were obtained from Sigma-Aldrich (USA). Terephthalic acid (H_2BDC, ≥ 98%) was purchased from Himedia (India), and N,N-dimethylformamide (DMF, 99.8%) was supplied by VN-CHEMSOL (Vietnam). OTC ($C_{22}H_{24}N_2O_9$, ≥ 98%), used as the target antibiotic, was sourced from MedChemExpress (USA). CNCs were prepared in-house via acid hydrolysis from the aerenchyma tissue of Neptunia oleracea, following the procedure described in our other work. Deionized water with a conductivity ≤ 0.05 μS/cm was prepared using a Milli-Q purification system.

The Fe_3O_4@CNCs composite was synthesized via a co-precipitation method based on the procedure reported by Janicijevic et al. (2021) [27]. The morphological features of the synthesized materials were investigated using scanning electron microscopy (SEM, model JSM-IT200, Jeol, Japan). Elemental composition was determined through energy-dispersive X-ray spectroscopy (EDS) integrated with the SEM system. Functional groups were identified via Fourier-transform infrared (FTIR) spectroscopy, performed on a Tensor 27 spectrometer (Bruker, Germany). Crystallographic characteristics were assessed by X-ray diffraction (XRD) using a LabX XRD-

6100 instrument (Shimadzu, Japan). Surface area and pore characteristics were measured through nitrogen adsorption–desorption isotherms using the Brunauer–Emmett–Teller (BET) method on a TriStar II Plus 3.03 analyzer (Micromeritics, USA). Magnetic properties were analyzed using a vibrating sample magnetometer (VSM, model EZ9, Microsense, USA). UV–visible spectral analysis was conducted with a Cary 3500 UV–Vis spectrophotometer (Agilent Technologies, USA).

The removal efficiency of Fe_3O_4@CNCs toward OTC was systematically examined by varying key operational parameters, including adsorbent mass, initial contaminant concentration, *pH*, contact duration, and temperature. To evaluate the impact of dosage and OTC levels, 5, 10, 20, and 30 mg of Fe_3O_4@CNCs were dispersed in 50 mL of OTC solutions at concentrations of 10, 20, 30, and 40 mg/L, contained in 100 mL Erlenmeyer flasks. Solution *pH* was adjusted within the range of 2–8 using 0.1 M nitric acid (HNO_3) or sodium hydroxide (NaOH). The samples were stirred at 250 rpm across controlled temperatures of 30, 40, 50, and 60 °C for various time intervals (5, 15, 30, 45, 60, 90, 120, and 150 minutes). At each designated time point, a neodymium magnet was applied to settle the magnetic adsorbent. The resulting supernatant was carefully collected and centrifuged at 4000 rpm for 2 minutes to remove any remaining suspended solids. The concentration of unadsorbed OTC was quantified by measuring the absorbance at 355 nm using a UV–visible spectrophotometer.

The equilibrium adsorption capacity (q_e, mg/g) was determined using equation (eq 1):

$$q_e = \frac{(C_0 - C_e).V}{m} \quad (1)$$

where C_0 and C_e (mg/L) represent the initial and equilibrium concentrations of OTC, respectively; V (L) is the solution volume, and m (g) denotes the mass of adsorbent used.

To evaluate the adsorption at any given time (q_t, mg/g), equation (eq 2) was applied:

$$q_t = \frac{(C_0 - C_t).V}{m} \quad (2)$$

with C_t (mg/L) indicating the concentration of OTC at time *t*.

The percentage removal efficiency (*R*, %) was calculated based on equation (eq 3):

$$R = \frac{C_0 - C_t}{C_0}.100\% \quad (3)$$

After identifying the optimal conditions for OTC adsorption by Fe_3O_4@CNCs, a comparative study was conducted to evaluate the adsorption capacities of CNCs, Fe_3O_4, and Fe_3O_4@CNCs. For this, 20 mg of each material was added to 50 mL of 20 mg/L OTC solution at *pH* 6 under ambient temperature.

After adsorption, the retained oxytetracycline was desorbed using 0.2 M HCl by shaking at 200 rpm for 120 minutes. A magnet was placed at the bottom of the Erlenmeyer flask to separate the magnetic adsorbent, and the supernatant was collected to measure the absorbance at 355 nm for quantifying desorbed OTC. Following desorption, the Fe_3O_4@CNCs composite was recovered, rinsed with deionized water until neutral *pH*, and dried at 50 °C. This adsorption–desorption cycle was repeated until the material showed no further reusability. Adsorption and desorption efficiencies were recorded and evaluated after each cycle.

3. RESUILS AND DISCUSSION

3.1. Characterization of Fe_3O_4@CNCs

The mixture of $FeSO_4 \cdot 7H_2O$ and $FeCl_3 \cdot 6H_2O$ salts was precipitated onto a nanocellulose matrix at a mass ratio of Fe_3O_4 to CNCs of 1:5. The resulting product was a black-brown solid with observable magnetic properties.

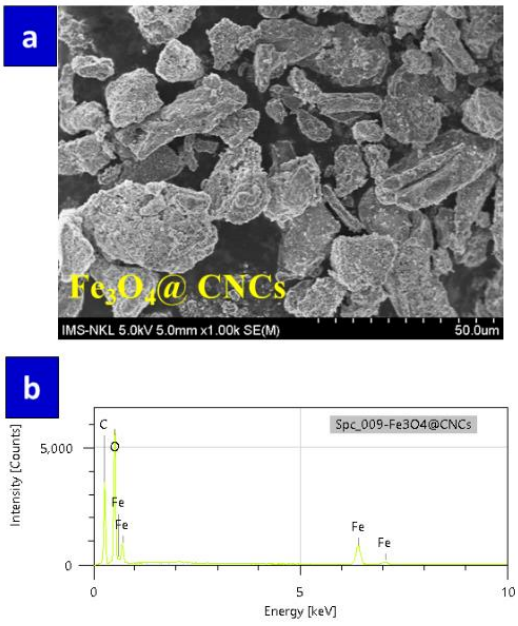

Figure 1. *(a) SEM images and (b) EDS spectrum of Fe_3O_4@CNCs.*

The successful fabrication of the Fe_3O_4@CNCs composite was confirmed by a combination of morphological, structural, chemical, and magnetic analyses. SEM image (Figure 1a) revealed a uniform distribution of Fe_3O_4 nanoparticles on the nanocellulose surface, with particle sizes ranging from 81.03 to 149.4 nm, indicating effective nucleation and stabilization facilitated by hydroxyl groups on CNCs. EDS analysis (Figure 1b) verified the presence of C (44.91%), O (47.47%), and Fe (7.62%), consistent with the expected composite composition.

The XRD pattern of the Fe_3O_4@CNCs composite (Figure 2a) confirmed the coexistence of both nanocellulose and Fe_3O_4 phases. Characteristic peaks of cellulose Iβ were observed at $2\theta \approx 15{,}6°$ (1̄10), 22,5° (200), and 34,5° (004), corresponding to the crystalline structure of CNCs (JCPDS No. 00-060-1502). Simultaneously, distinct peaks at $2\theta \approx$ 30,2° (220), 35,6° (311), 43,2° (400), 57.2° (511), and 62,8° (440) matched well with the standard cubic spinel structure of Fe_3O_4 (JCPDS No. 19-0629), indicating the presence of the magnetite phase with high crystallinity. These findings collectively confirmed the successful incorporation of Fe_3O_4 nanoparticles into the nanocellulose matrix.

FT-IR spectroscopy (Figure 2b) further supported the formation of the composite. The spectrum exhibited the typical absorption bands of cellulose (O–H, C–H, C=O, and C–O stretching), while Fe_3O_4 contributed a prominent Fe–O band at 580 cm^{-1}. A red shift in the O–H stretching vibration in the composite suggested hydrogen bonding between Fe_3O_4 and the cellulose surface, indicating strong interfacial interaction.

BET surface area analysis (Figure 2c) revealed a specific surface area of 6.3350 ± 0.0713 m^2/g, based on a slope of 0.6858 and an intercept of 0.00127 from the nitrogen adsorption isotherm. This moderately high surface area suggested the development of a porous structure, favorable for enhanced adsorption and surface-driven processes.

Magnetic characterization (Figure 2d) demonstrated superparamagnetic behavior. While the saturation magnetization of pure Fe_3O_4 reached 82.52 emu/g, it decreased to 14.91 emu/g in the composite due to dilution by non-magnetic cellulose. Nevertheless, the magnetic response was adequate for rapid magnetic separation, highlighting the

composite's potential for reusable adsorbent applications, such as OTC removal from aqueous systems.

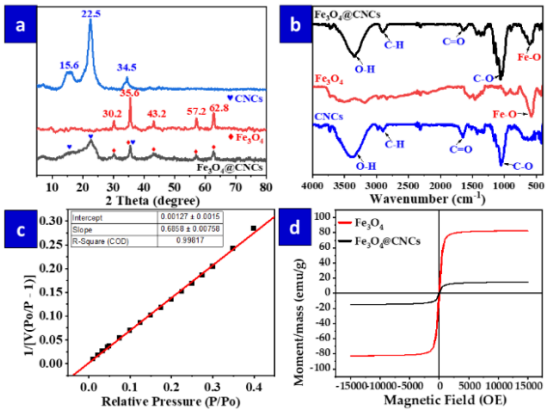

Figure 2. *(a) XRD patterns; and (b) FTIR spectra of CNCs; Fe_3O_4; and Fe_3O_4@CNCs. (c) BET surface area plot; and (d) VSM curves with magnetic separation inset of Fe_3O_4@CNCs.*

3.2. Adsorption Performance Evaluation

Effect of adsorption time. Figure 3a showed that OTC removal increases rapidly within the first 60 minutes, followed by a gradual plateau, reaching equilibrium at 150 minutes with a maximum q_e of 27.40 mg/g and removal efficiency R of 51.25%. This indicated rapid initial occupation of active sites on the composite surface.

Effect of adsorbent dosage. As shown in Figure 3b, increasing the adsorbent dosage from 5 to 30 mg reduced q_e (50.18 to 21.11 mg/g) but enhanced R (20.25% to 60.69%). This trend reflected a greater number of available active sites, though excessive dosage might lead to site aggregation and underutilization.

Effect of OTC concentration. Figure 3c illustrated that q_e increased from 18.76 to 38.43 mg/g as OTC concentration rose from 10 to 40 mg/L, while R declined from 73.59% to 36.06%. The decline in R was attributed to surface site saturation and increased molecular interactions hindering further adsorption.

Effect of pH. The point of zero charge (pH_pzc) of Fe_3O_4@CNCs was determined to be 5.9 (Figure 4a). Below this *pH*, the surface was positively charged; above it, negatively charged. Since OTC formed anionic species at higher *pH*, electrostatic repulsion reduced adsorption. As shown in Figure 4b, optimal adsorption occured at pH 6 (R = 89.08%, q_e = 22.83 mg/g). Deviation from this *pH* led to diminished performance due to charge repulsion and reduced electrostatic attraction.

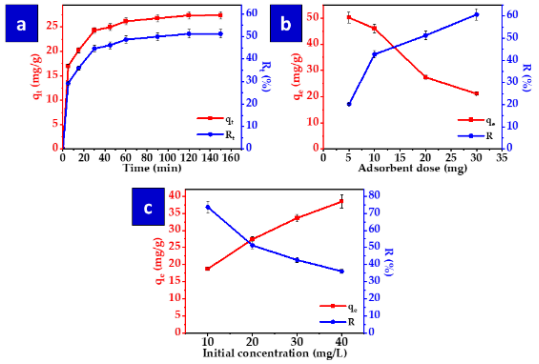

Figure 3. *Adsorption performance evaluation Fe_3O_4@CNCs: (a) Effect of contact time; (d) Effect of adsorbent dosage; and (c) Effect of OTC concentration.*

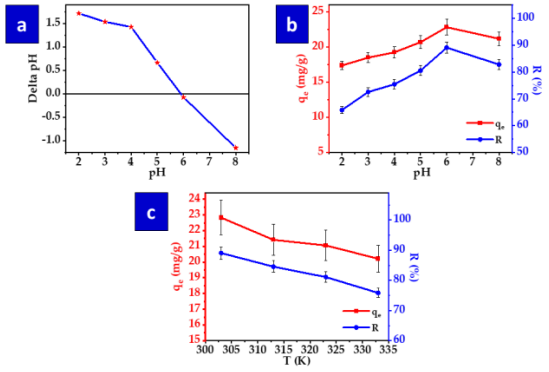

Figure 4. *Adsorption performance evaluation Fe_3O_4@CNCs: (a) Point of zero charge (pH_pzc) of the material; (b) Effect of pH; and (c) Effect of temperature.*

Effect of temperature. Figure 4c indicated that room temperature (30 °C) yields the highest R (89.08%) and q_e (22.83 mg/g).

Higher temperatures (40–60 °C) caused a slight decline in both metrics, suggesting the process was exothermic and more favorable at ambient conditions.

Evaluation of Adsorption Capacity and Reusability. Figure 5a showed that Fe_3O_4@CNCs exhibited superior OTC removal efficiency compared to pristine CNCs under identical conditions (303 K, *pH* 6, 20 mg adsorbent, 120 minutes, 20 mg/L OTC). The poor performance of CNCs was likely due to limited pore size and unfavorable surface interactions with OTC molecules. In contrast, Fe_3O_4 functionalization improved both pore accessibility and chemical affinity, resulting in significantly enhanced adsorption performance. To assess reusability, the Fe_3O_4@CNCs composite was subjected to four consecutive adsorption–desorption cycles. As shown in Figure 3b, 0.2 M HCl achieved high desorption efficiency, reaching 97.66% after 120 minutes. The composite maintain high removal efficiency during the first three cycles (84.15%, 80.09%, and 70.11%, respectively), before declining to 53.95% in the fourth cycle. This trend suggested a gradual reduction in performance, likely due to deactivation of active sites, pore blockage, or irreversible adsorption of OTC molecules. Nonetheless, the material exhibited robust recyclability with >70% removal efficiency over three reuse cycles, indicating its practical applicability in wastewater treatment. XRD and FT-IR analyses (Figures 5c and 5d) revealed no major structural changes in the composite after four cycles. Characteristic peaks of Fe_3O_4 and nanocellulose remained, with only minor intensity reductions likely due to iron leaching and material loss. These results confirmed the composite's excellent phase stability and structural resilience, underscoring its potential for repeated use in environmental applications.

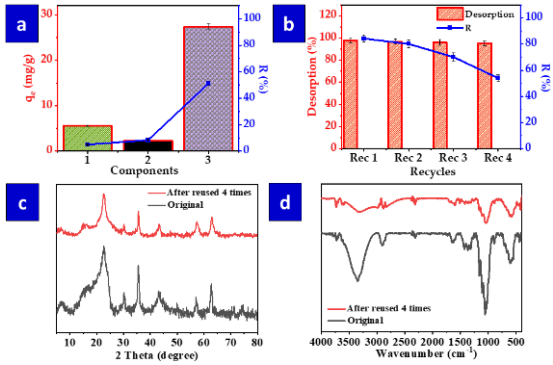

Figure 5 *(a) Dual-column bar chart illustrating qe and removal of the material components; (b) Desorption and reusability of Fe_3O_4@CNCs for OTC adsorption; (c) XRD patterns and (d) FTIR spectra illustrating the crystalline structures of Fe_3O_4@CNCs before use and after four reuse cycles.*

3.3. Kinetic Studies

The adsorption mechanism of oxytetracycline (OTC) onto Fe_3O_4@CNCs was investigated by fitting experimental data to the pseudo-first-order (PFO), pseudo-second-order (PSO), and Weber–Morris intraparticle diffusion models. The respective linearized forms were:

PFO model (eq 4):

$$\ln(q_e - q_t) = \ln(q_e) - k_1 t \quad (4)$$

PSO model (eq 5):

$$\frac{t}{q_t} = \frac{1}{k_2 q_e^2} + \frac{t}{q_e} \quad (5)$$

Weber-Morris model (eq 6):

$$q_t = k_{dif}.t^{\frac{1}{2}} + C \quad (6)$$

where k_1 (min^{-1}) was the PFO rate constant, k_2 ($g/mg.min^{-1}$) was the PSO rate constant, k_{dif} ($mg/g \cdot min^{1/2}$) was the intraparticle diffusion rate constant, $t^{1/2}$ ($min^{1/2}$) was the square root of time, and C (mg/g) was the constant related to the thickness of the boundary layer.

By applying linear regression to the kinetic data at an initial OTC concentration of 10 mg/L, the parameters q_e, k_1, and k_2 were estimated, and model fitting is evaluated using the coefficient of determination (R^2) and residual sum of squares (*RSS*), as shown in Table 2.

Table 2. *Comparison of pseudo-first-order (PFO) and pseudo-second-order (PSO) kinetic parameters.*

OTC Concentration (mg/L)	$q_{e,\,exp}$ (mg/g)	Kinetic model	$q_{e,\,cal}$ (mg/g)	k	R^2
10	22.83	PFO	5.28	0.0235	0.9919
		PSO	22.89	0.0147	0.9994

The PFO model (Figure 6a) yields an R^2 of 0.9919 and significantly underestimated the equilibrium adsorption capacity compared to experimental data, indicating a poor fit. In contrast, the PSO model (Figure 6b) produced an R^2 of 0.9994 and a calculated q_e value closely matching the experimental result, demonstrating superior agreement. These findings suggested that the OTC adsorption process followed pseudo-second-order kinetics, governed primarily by chemisorption rather than degradation.

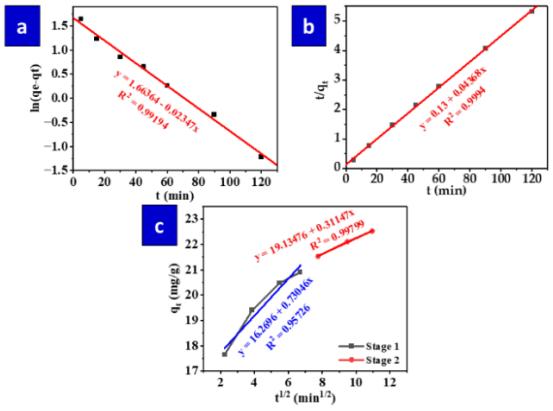

Figure 6. *Linear fitting of the adsorption kinetics of OTC onto Fe_3O_4@CNCs using (a) the Pseudo-first-order kinetic model; (b) the Pseudo-second-order kinetic model; and (c) the Weber-Morris intraparticle diffusion model*

As shown in Figure 6c, the intraparticle diffusion plot revealed a two-stage adsorption process. The first stage (within the initial 45 minutes) corresponded to rapid external surface adsorption of OTC, followed by a second stage involving slower diffusion into the internal pores and interaction with active sites. The extended duration of the second stage might be attributed to the relatively large molecular structure of OTC, which limited its penetration into the adsorbent's porous network.

3.4. Adsorption Isotherms

To elucidate the adsorption behavior of OTC on Fe_3O_4@CNCs, the Langmuir and Freundlich isotherm models were applied. The Langmuir model assumed monolayer adsorption on a homogeneous surface and is expressed linearly (eq 7) as:

$$\frac{C_e}{q_e} = \frac{1}{q_{max}.K_L} + \frac{C_e}{q_{max}} \quad (7)$$

In contrast, the Freundlich model described adsorption on heterogeneous surfaces with the formation of multilayer adsorption, represented by the equation (eq 8):

$$\log q_e = logK_F + \frac{1}{n} logC_e \quad (8)$$

where q_{max} (mg/g) was the maximum adsorption capacity, K_L (L/mg) was the Langmuir adsorption constant, K_F (mg/g.(L/mg)$^{1/n}$) was the Freundlich constant related to adsorption capacity, and n (dimensionless) was the Freundlich exponent indicating the favorability of the adsorption process.

As shown Figures 7a and 7b, both Langmuir and Freundlich isotherm models fit the experimental data well, with high correlation coefficients (R^2 > 0.98). The Langmuir model yields R^2 = 0.9876, while the Freundlich model

achieved a better fit with R^2 = 0.9987. In the Freundlich model, the exponent *n* was greater than 1, indicating surface heterogeneity and favorable multilayer adsorption across the tested concentration range. This supported the assumption that each adsorption site could accommodate more than one OTC molecule. The Langmuir model also demonstrated good agreement, as the calculated separation factor (R_L) values range from 0.0056 to 0.0222, which fell within the favorable range ($0 < R_L < 1$). Overall, the adsorption of OTC onto Fe_3O_4@CNCs was consistent with both Langmuir and Freundlich isotherm behaviors.

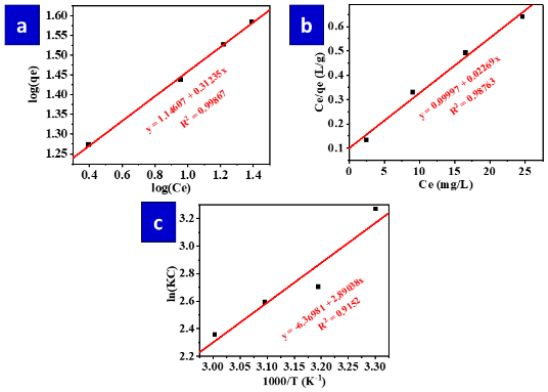

Figure 7. *Linear regression curves fitted to (a) the Freundlich and (b) Langmuir isotherm models for OTC adsorption. (c) Plot of ln(K_C) versus 1000/T.*

3.5. Adsorption Thermodynamics

Thermodynamic studies were performed to elucidate the adsorption mechanism of OTC onto Fe_3O_4@CNCs using key parameters: Gibbs free energy (ΔG), enthalpy (ΔH), and entropy (ΔS). These values were derived from adsorption experiments conducted at various temperatures, based on the linearized Van't Hoff equation (eq 9):

$$\ln(K_C) = -\frac{\Delta H}{R}.\frac{1}{T} + \frac{\Delta S}{R} \quad (9)$$

The corresponding Gibbs free energy at each temperature (eq 10) was calculated using:

$$\Delta G = \Delta H - T.\Delta S \quad (10)$$

Thermodynamic parameters (Table 3 and Figure 7c) confirm that OTC adsorption onto Fe_3O_4@CNCs was spontaneous and exothermic. The negative ΔG values (–7.98 to –6.40 kJ/mol) across 303.15–333.15 K indicated favorable adsorption, though decreasing ΔG with increasing temperature suggested reduced spontaneity at higher temperatures. The enthalpy change (ΔH = –24.03 kJ/mol) fell within the range for physisorption, implying that weak interactions such as hydrogen bonding and van der Waals forces dominate. The negative entropy change (ΔS = –52.96 J/mol·K) reflected decreased randomness due to OTC immobilization on the surface and restructuring of interfacial water. Overall, the adsorption was a mildly exothermic physisorption process, consistent with the slight decline in efficiency at elevated temperatures.

Table 3. *Thermodynamic parameters of OTC adsorption onto Fe_3O_4@CNCs*

Temperature (K)	ΔG (kJ/mol)	ΔH (kJ/mol)	ΔS (J/mol.K)	R^2
303	-7.98	-24.03	-52.96	0.9152
313	-7.45			
323	-6.92			
333	-6.40			

4. CONCLUSION

This study demonstrated the successful synthesis of a magnetic nanocellulose-based adsorbent (Fe_3O_4@CNCs) with uniformly distributed Fe_3O_4 nanoparticles, a porous architecture, and superparamagnetic behavior (M_s = 14.91 emu/g). The composite exhibited excellent performance for oxytetracycline (OTC) removal, achieving a monolayer adsorption capacity of 50.76 mg/g (Langmuir model). Under optimal

conditions (pH 6, 30 °C, 20 mg adsorbent, 10 mg/L OTC), it reached a removal efficiency of 89.08% and an adsorption capacity (q_e) of 22.83 mg/g. Adsorption kinetics followed a pseudo-second-order model (R^2 = 0.9994), indicating chemisorption as the dominant mechanism. Thermodynamic parameters (ΔG, ΔH, ΔS < 0) confirmed that the process was spontaneous, exothermic, and primarily driven by physical interactions such as hydrogen bonding and van der Waals forces. After three consecutive adsorption–desorption cycles, the material maintained a removal efficiency above 70%, and FTIR and XRD analyses showed no significant structural degradation. These results highlighted the potential of Fe_3O_4@CNCs as a reusable, magnetically separable, and eco-friendly adsorbent for the remediation of antibiotic-contaminated water.

Acknowledgments: The authors would like to express their sincere gratitude to Industrial University of Ho Chi Minh City for providing the necessary facilities and support to complete this research.

REFERENCES

[1] C. Monahan, S. Harris, D. Morris, and E. Cummins, (2022). A comparative risk ranking of antibiotic pollution from human and veterinary antibiotic usage – An Irish case study. *Science of The Total Environment,* **(826)**, 154008, 2022/06/20/ 2022.

[2] H. Zeng *et al.*, (2022). The Current Status and Prevention of Antibiotic Pollution in Groundwater in China. *International Journal of Environmental Research and Public Health,* **19**.

[3] B. Zhao, P. M. van Bodegom, and K. B. Trimbos, (2023). Antibiotic Resistance Genes in Interconnected Surface Waters as Affected by Agricultural Activities. *Biomolecules,* **2(13)**.

[4] D. Baral, A. Bhattarai, and N. K. Chaudhary, (2024). Aquifer pollution by metal-antibiotic complexes: Origins, transport dynamics, and ecological impacts. *Ecotoxicology and Environmental Safety,* **(288)**, 117390.

[5] M. Watanabe *et al.*, (2023). Occurrence and the potential ecological risk of veterinary antimicrobials in swine farm wastewaters in Japan: Seasonal changes, relation to purchased quantity and after termination of oxytetracycline usage. *Environment International,* **(173)**, 107812.

[6] R. Xiao, D. Kang, H. Zhao, M. Fan, Y. Peng, and J. Niu, (2024). Metagenomic Insights into the Microbial Community of Activated Sludge in Oxytetracycline Wastewater Treatment. *Water,* **24(16)**.

[7] H.-Y. Chen *et al.*, (2022). The fate and behavior mechanism of antibiotic resistance genes and microbial communities in anaerobic reactors treating oxytetracycline manufacturing wastewater. *Journal of Hazardous Materials,* **(424)**, 127352.

[8] S. Karmakar *et al.*, (2024). The role of environmentally relevant concentrations of oxytetracycline in the emergence of antimicrobial resistance in Aeromonas hydrophila and Edwardsiella tarda. *Journal of Hazardous Materials Letters,* **(5)**, 100130.

[9] Y. He, Z. Tian, X. Luan, Z. Han, Y. Zhang, and M. Yang, (2021). Recovery of biological wastewater treatment system inhibited by oxytetracycline: Rebound of functional bacterial population and the impact of adsorbed oxytetracycline on antibiotic resistance. *Chemical Engineering Journal,* **(418)**, 129364.

[10] Y. Zhang, J. Li, Z. Hu, J. Li, and H. Lu, (2022). Oxytetracycline stress stimulates antibiotic resistance gene proliferation and quorum sensing response of marine anammox bacteria in seawater-based

wastewater treatment. *Chemical Engineering Journal*, **(447)**, 137539.

[11] M. Xia *et al.*, (2023). Simultaneous adsorption and biodegradation of oxytetracycline in wastewater by Mycolicibacterium sp. immobilized on magnetic biochar. *Environmental Pollution*, **(339)**, 122728.

[12] D. T. C. Nguyen *et al.*, (2011). Box–Behnken design, kinetic, and isotherm models for oxytetracycline adsorption onto Co-based ZIF-67. *Applied Nanoscience*, **8(11)**, 2347-2359.

[13] R. Kumar *et al.*, (2022). Integrated Adsorption-Photocatalytic Decontamination of Oxytetracycline from Wastewater Using S-Doped TiO2/WS2/Calcium Alginate Beads. *Catalysts*, **12(12)**.

[14] Y. Fan *et al.*, (2023). Removal of oxytetracycline from wastewater by biochar modified with biosynthesized iron oxide nanoparticles and carbon nanotubes: Modification performance and adsorption mechanism. *Environmental Research*, **(231)**, 116307.

[15] A. Hammari, U. Hamza, M. Ibrahim, K. Garba, I. Muhammad, and O. Oludoye, (2024). Innovative Application of Cellulose Nano-crystals from Agricultural Waste for Enhanced Pharmaceutical Wastewater Treatment through Artificial Intelligence-Driven Adsorption Modelling. *Global Journal of Environmental Science and Sustainability*.

[16] W. Jiang, Y. Cai, D. Liu, X. Yu, and Q. Wang, (2024). Enhanced adsorption performance of oxytetracycline in aqueous solutions by Mg-Fe modified suaeda-based magnetic biochar. *Environmental Research*, **(241)**, 117662.

[17] A. S. Norfarhana *et al.*, (2024). Exploring of Cellulose Nanocrystals from Lignocellulosic Sources as a Powerful Adsorbent for Wastewater Remediation. *Journal of Polymers and the Environment*, **9(32)**, 4071-4101.

[18] A. I. A. Soliman, J. A. Díaz Baca, and P. Fatehi, (2023). One-pot synthesis of magnetic cellulose nanocrystal and its post-functionalization for doxycycline adsorption. *Carbohydrate Polymers*, **(308)**, 120619.

[19] L. S. Mesoppirr, S. E. K., O. W. N., O. N. M., and S. M. and Nelana, (2024). Preparation and characterization of β-cyclodextrin capped magnetic nanoparticles anchored on cellulosic matrix for removal of cr(VI) from mimicked wastewater: Adsorption and kinetic studies. *Journal of Environmental Science and Health, Part A*, **9(59)**, 472-487.

[20] W. Xiong, K. Tian, S. Liu, M. Li, and Y. Zhu, (2025). TEPA modified magnetic cellulose nanocrystals for efficient and highly selective removal of Cr(VI) from electroplating wastewater by high-density amine-based sites. *Journal of Colloid and Interface Science*, **(685)**, 1195-1208.

[21] C. Hou *et al.*, (2021). Core–shell magnetic Fe3O4/CNC@MOF composites with peroxidase-like activity for colorimetric detection of phenol. *Cellulose*, **14(28)**, 9253-9268.

[22] R. Amen, I. Elsayed, G. T. Schueneman, and E. B. Hassan, (2024). Self-Assembled Aminated and TEMPO Cellulose Nanofibers (Am/TEMPO-CNF) Aerogel for Adsorptive Removal of Oxytetracycline and Chloramphenicol Antibiotics from Water. *Gels*, **(10)**.

[23] A. El Nemr, A. A. M. El-Assal, A. El Sikaily, M. E. Mahmoud, M. F. Amira, and S. Ragab, (2021). New magnetic cellulose nanobiocomposites for Cu(II), Cd(II) and Pb(II) ions removal: kinetics, thermodynamics and analytical evaluation. *Nanotechnology for Environmental Engineering*, **3(6)**, 42.

[24] D. Zhao *et al.*, (2022). Tetraethylenepentamine modified magnetic cellulose nanocrystal composites for removal of Congo red with high adsorption capacity. *Journal of Dispersion Science and Technology,* **12(43)**, 1858-1871.

[25] T. Su *et al.*, (2024). Cellulose nanocrystal-based polymer hydrogel embedded with iron oxide nanorods for efficient arsenic removal. *Carbohydrate Polymers,* **(331)**, 121855.

[26] Q. Zhang *et al.*, (2024). Effect on the adsorption performance and mechanism of antibiotics tetracyclines by the magnetic biochar used peanut shells as raw materials. *Materials Research Express,* **4(11)**, 045508.

[27] A. Janićijević, A. Sknepnek, M. M. Mirković, V. B. Pavlović, and S. J. T. Filipović, (2021). Optimization of the synthesis parameters of nanocomposites based on bacterial nanocellulose/Fe3O4.